GEOPHYSICS, VOL. 90, NO. 4 (JULY-AUGUST 2025); P. G93–G108, 14 FIGS.
10.1190/GEO2024-0005.1

Enabling small anomaly detection using finite-difference magnetic gradiometry

Heidi Myers[1], Daniel Lathrop[2], and Vedran Lekic[3]

ABSTRACT

Magnetometry is used to detect ferrous objects at various scales but detecting small-size compact sources that produce small-amplitude anomalies in the shallow subsurface remains challenging. Magnetic anomalies are often approximated as dipoles or volumes of dipoles that can be located, and their source parameters (burial depth, magnetization direction, magnetic susceptibility, etc.) are characterized using scalar or vector magnetometers. Both types of magnetometers are affected by space weather and cultural noise sources that map temporal variations into spatial variations across a survey area. The vector magnetometers provide more information about detected bodies at the cost of extreme sensitivity to orientation, which cannot be reliably measured in the field. Magnetic gradiometry addresses the problem of temporal-to-spatial mapping and reduces distant noise sources but the heading error challenges remain, motivating the need for magnetic gradient tensor (MGT) invariants that are relatively insensitive to rotation. Here, we show that the finite size of magnetic gradiometers compared with the length-scales of magnetic anomalies due to small buried objects affects the properties of the gradient tensor, such as symmetry and invariants. This renders traditional assumptions of magnetic gradiometry largely inappropriate for detecting and characterizing small-size anomalies. We then show how the properties of the finite-difference MGT and its invariants can be leveraged to map these small sources in the shallow critical zone, such as unexploded ordnance, landmines, and explosive remnants of war, using synthetic and field data obtained with a triaxial magnetic gradiometer (TetraMag).

INTRODUCTION

Magnetometry is a ubiquitous geophysical technique used to detect magnetic anomalies produced by various sources, such as ore bodies (Azry et al., 1993; Gunn and Dentith, 1997; Hinze et al., 2013; Shahsavani, 2019), igneous intrusions (Nogi et al., 1995; Santos et al., 2019; Michelena et al., 2022; Accomando et al., 2023), subsurface structures (Birch, 1984; Cordell and Grauch, 1985; Barrère et al., 2011; Døssing et al., 2013), and, for some humanitarian geophysics applications, landmines and unexploded ordnance (UXO) (Yoo et al., 2020; Accomando et al., 2021; Alqudsi et al., 2021). These magnetic anomalies are often approximated as dipoles or volumes of dipoles (Blakely, 1995; Hamlyn, 2022), and locating and inferring their characteristics, such as burial depth and magnetic moment, is challenging, regardless of whether using data from scalar or vector magnetometers. Geologic-scale features traditionally of interest span spatial dimensions of hundreds of meters to hundreds of kilometers and produce anomalies on the order of tens to hundreds of nanotesla (Florsch et al., 2018). In contrast, magnetic anomalies produced by landmines and UXO are typically between 0.05 m and 2 m in spatial extent and produce anomalies on the order of tens of nT to hundreds of nT (Nikulin et al., 2020; Yoo et al., 2021).

Surveys to detect larger geologic magnetic anomalies typically use scalar magnetometers and are often performed aerially. Surveys to detect small compact sources such as landmines and UXO use scalar and vector magnetometers and are most often ground-based, though efforts to integrate magnetometers on helicopters or unmanned aerial vehicles (UAVs) for landmine and UXO detection have gained traction over the past decade (Munschy et al., 2007; Gavazzi et al., 2016; Zuo et al., 2017; Baur et al., 2020; Mu et al., 2020; Barnawi et al., 2022).

Manuscript received by the Editor 3 January 2024; revised manuscript received 26 January 2025; published ahead of production 5 March 2025; published online 6 May 2025.
[1]The Johns Hopkins University, Applied Physics Laboratory, Laurel, Maryland, USA and University of Maryland, Institute for Research in Electronics and Applied Physics (IREAP), College Park, Maryland, USA. E-mail: hpm@umd.edu (corresponding author).
[2]University of Maryland, Institute for Research in Electronics and Applied Physics (IREAP), College Park, Maryland, USA and University of Maryland, Department of Geology, College Park, Maryland, USA. E-mail: lathrop@umd.edu.
[3]University of Maryland, Department of Geology, College Park, Maryland, USA. E-mail: ved@umd.edu.

In this study, we focus on small buried objects in the shallow critical zone ranging from infrastructure to landmines, which necessitates the characterization of the small-amplitude anomalies produced by these sources. This task comes with unique challenges for survey methodology and instrumentation selection, which affect the fidelity and interpretability of collected data. First, we discuss the advantages and disadvantages of scalar and vector magnetometry in this context before turning our attention to how magnetic gradiometry can overcome many of the disadvantages. We then focus on the quantitative characteristics of finite difference versus infinitesimal magnetic gradient tensors (IMGT) in the context of this challenge, and analyze how they relate to the physical dimensions of the gradiometer, as well as the distance and azimuth from the source. We explore the utility of several magnetic gradient tensor (MGT) invariants for source localization (defining the source's coordinate position as seen on a map) and then compare their performance under rotation using synthetic data. Finally, we demonstrate the gradient tensor and its invariants using field data for a small dipole-like source buried at 15 cm depth.

Challenges of scalar, vector, and gradient magnetometry

Scalar magnetometry

Scalar magnetometers are the standard tool used for ground-based and aerial surveys due to their high sensitivity and ease of data analysis. Sensor height plays a key limiting role when targeting small-amplitude shallow anomalies such as landmines and UXO, independent of the sensor's sensitivity. Figure 1 shows the expected total field magnetic anomaly for a dipole-like antitank (AT) landmine buried at 15 cm depth, as measured from various sensor heights. As the magnetometer height increases, signals from geomagnetic storms and/or nearby direct current (DC) metro systems completely obfuscate the amplitude of the AT mine, increasing the

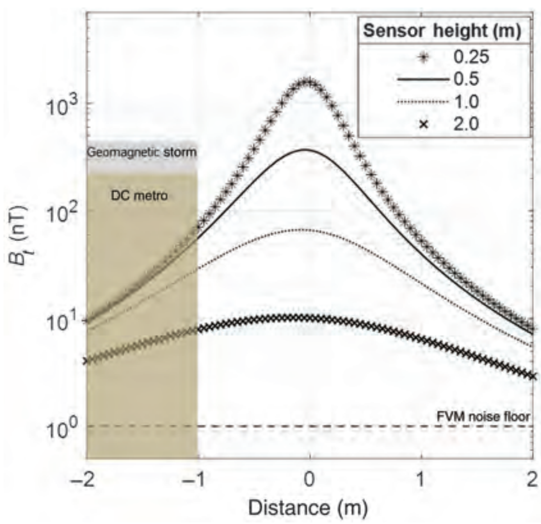

Figure 1. Expected magnetic total field anomaly (B_t) of a dipole-like AT mine buried at 15 cm depth measured from various sensor heights above ground level, compared with typical amplitudes of geomagnetic storms and nearby DC metro systems (shaded areas) and the noise floor of the magnetometer used in this study, MEDA FVM400 (dashed line). At height >0.5 m, geomagnetic storms and DC metro signals can obfuscate the AT mine, producing false flags.

chance of false flags. Antipersonnel (AP) landmines and cluster munitions of a similar size will have even smaller signatures. This is particularly important for UAV-based surveying and surveys carried out near urban environments with DC metro systems.

Crucially, scalar measurement magnitudes do not depend on instrument orientation, except when the sensor enters a dead zone. This facilitates observations when precise pointing control is difficult to achieve, which is the case in typical field conditions, especially when flying. Their high sensitivity enables scalar magnetometers to easily record temporal variations in magnetic field strength caused by space weather and cultural noise sources.

Limited information content of scalar measurements makes it difficult to reliably estimate parameters (burial depth, magnetization direction, etc.) beyond the surface map location of small-size low-amplitude sources. Depth estimates for large-scale anomalies can be made from total field data by relying on graphical and analytical methods developed by Peters (1949), Bott and Smith (1958), and Smith (1959). Peters' method is suboptimal for small-scale surveys involving small-size anomalies because it requires many simplifying assumptions to be made about the source, including having uniform magnetization and vertical sides with a large depth extent, and requires magnetic contour maps whose spacings are equal and proportional to the depth of the source (Blakely, 1995). Maximum depth rules derived by Bott and Smith are best suited when the anomaly is caused by an isolated single source, which is not the case for many minefields, nor most real-world geologic situations. Euler and Werner deconvolution can be used to approximate depths when there are many sources (or volumes of sources) of simple shape but work best when the sources are sufficiently isolated, and results are very sensitive to noise (Thompson, 1982; Reid et al., 1990). In addition, Euler's method requires information about the source directional gradients, which are not directly sampled using scalar magnetometers but instead calculated in the Fourier domain using multiple filtering operations that can be unstable depending on survey spacing and the orientation of the source magnetization vector and ambient field vector (Blakely, 1995).

Scalar field measurements by nature contain less information about source magnetic susceptibility, shape, and orientation, making interpretations difficult as their inversions are highly nonunique when used in isolation. Some of the nonuniqueness can be reduced by jointly inverting with other data types or introducing known priors (Zeyen and Pous, 1993; Gallardo et al., 2012; Ghalenoei et al., 2021). For compact small-amplitude sources such as landmines and UXO, there is an additional challenge of distinguishing the sources of interest from metallic clutter or shrapnel, and inversion methods using total field data rely on approximating the octupole component of a simplified spheroid, or assuming an arbitrarily axially symmetric body and attempting to recover the dipole and quadrupole moments from it (Billings et al., 2002; Pasion et al., 2003). Although transformations can be applied to total field measurements to approximate vector components, the operations become unstable depending on the direction of the ambient field (Blakely, 1995). In addition, any instrument noise will map to spurious artifacts during scalar-to-vector component transformations (Liu et al., 2022).

This motivates the use of vector magnetometers, which can provide up to three times as much information about buried objects, such as sensitivity to their orientation and shape, more directly than using total field data transformations to approximate vector components.

Vector magnetometry

Vector magnetometers provide greater utility and benefit from being lightweight and field rugged. They also provide more information than scalar magnetometers by measuring vector components directly. Similar to scalar magnetometers, vector magnetometers suffer from the temporal-to-spatial variation mapping and sensor-height-to-signal-amplitude issues described in the previous section. In addition, they are exceedingly sensitive to pointing errors.

Here, pointing errors refer to the angular uncertainty in knowing the magnetometer's orientation in space compared with its actual position, not the inherent nonorthogonality of individual fluxgate sensors. Because a triaxial fluxgate magnetometer measures the local magnetic field with respect to the magnetometer's x-, y-, and z-axis, any uncertainty in the magnetometer position will result in the ambient field being mapped into the measured signals. We adopt the naming conventions of yaw (rotation about the z-axis), pitch (rotation about the x-axis), and roll (rotation about the y-axis) to describe these angular deviations.

Figure 2 shows signal error as the percentage of expected magnetic anomaly for the same AT mine in Figure 1, calculated for a triaxial fluxgate magnetometer from 0.5 m height, as a function of the yaw pointing error of the sensor. Here, B_x, B_y, and B_z represent the vector components of the expected magnetic anomaly, and ambient magnetic inclination and declination values are for College Park, Maryland. Even very small pointing errors (<1°) result in spurious magnetic signals that are large enough in amplitude to mimic those from the AT mine, increasing the chances of false flags. This relationship extends to any small dipole-like source, making precise pointing crucial for mapping their magnetic signatures.

However, maintaining subdegree pointing accuracy is an extremely difficult task for human-held fluxgate magnetometers and is practically untenable for ground-based or aerial vehicle systems, such as UAVs. Although the use of microelectromechanical system accelerometers can help determine the orientation of fluxgate magnetometer sensor heads for making corrections, achieving accuracies <1° is difficult in a dynamic environment (Pham and Desimone, 2017), and vibrations aboard crafts such as UAVs produce additional inaccuracies that can create spurious signals at the same scale as sources of interest. Although an inertial measurement unit (IMU) can be used to track these positional changes to make corrections, even small uncertainties in knowing the magnetometer's orientation can result in spurious signals that are beyond the ability to correct and of the same order of magnitude as anomalies produced by small-size small-amplitude sources.

Limitations are also associated with the fixed nonorthogonality and offset errors for each fluxgate sensor (Pang et al., 2013; Gavazzi et al., 2019). The measurement inaccuracies that arise when the three axes are not perfectly orthogonal when fabricating the fluxgate sensor necessitate careful calibration and correction procedures to ensure accurate magnetic field measurements. Field calibration efforts have been made to account for some of the sensitivities and offset errors (Merayo et al., 2000; Olsen et al., 2003; Pylvänäinen, 2008; Pang et al., 2013) but the pointing errors remain difficult to compensate for in human-held and vehicle-based magnetometer systems (Schmidt and Clark, 2006).

Mapping of temporal to spatial variations

Regardless of whether one uses scalar or vector magnetometers to carry out a magnetic survey where magnetic field strength measurements at different locations are made at different times, temporal variations in the magnetic field will map into spurious spatial variations.

Space weather is a common source of temporal magnetic field variations. The magnitude of space weather contributions can range from picotesla to hundreds of nanotesla scales under geomagnetically quiet conditions but variations of thousands of nanotesla can occur within minutes during very strong geomagnetic storms, such as from an impact of an coronal mass ejection on the Earth (Mandea and Chambodut, 2020). In addition, proximity to urban magnetic noise sources such as DC metro systems also produces temporal magnetic field variations, detrimentally impacting the ability to reliably map out anomalies at the scale of hundreds of nantesla (Kappler et al., 2017). Temporal variations from either source can result in spurious spatial signals that swamp out the expected amplitudes from small sources of interest. When mapping large-scale anomalies, these spurious signals can be partially corrected by applying diurnal corrections with a base station and/or subtracting the International Geomagnetic Reference Field model from the field data (Riddihough, 1971; Yarger et al., 1978; Foss, 2020). However, this will not remove interfering anomalies from local noise sources common in urban environments.

Although the precise mapping of temporal-to-spatial variations depends on the accuracy of the positioning system (global navigation satellite system or otherwise) and acquisition geometry, short-period variations generally map to small-scale structures. In contrast, long-period variations can map into either small- or large-scale structures. Scalar base station recordings are often used to correct spurious signals from total field and vector component magnetic data, especially in aeromagnetic and UAV-based surveys. However, it is important to note that the effectiveness of this approach depends on geomagnetic conditions. Figure 3 illustrates the differences between geomagnetically quiet and storm conditions in coherence between pairs of magnetic reference stations. During quiet conditions, coherence values

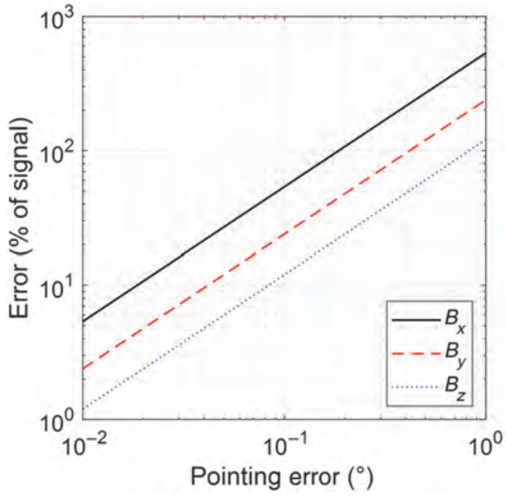

Figure 2. Signal error produced as the percentage of expected magnetic anomaly for a metal AT mine buried at 15 cm depth, measured with a triaxial fluxgate magnetometer from 0.5 m height, as a function of the uncertainty that arises from yaw pointing error (°) of the sensor. Here, $B_x = 150$ nT, $B_y = 200$ nT, $B_z = 400$ nT, declination = −10.5°, inclination = 67.12° (matching College Park, MD). Very small pointing errors produce spurious magnetic signals large enough to obscure those produced by the AT mine, increasing the chances of false flags.

decrease at higher frequencies, indicating suboptimal base-station data for short-period variations, whereas during a geomagnetic storm, enhanced coherence for north and east components. Differences in coherence between different pairs of magnetic field components can only be accounted for if one measures the vector components of the magnetic field, such as by using fluxgate triaxial magnetometers.

Magnetic gradiometry

Magnetic gradiometry largely solves the problem of temporal-to-spatial mapping because gradiometers are sensitive to nearby variations and relatively insensitive to distant variations (Schmidt and Clark, 2000). This is because the correlated signals produced by cultural and space weather can be effectively suppressed by differencing signals recorded at nearby magnetometers. For an infinitesimal triaxial gradiometer, this results in the nine-component IMGT $\hat{\mathbf{G}}$ represented as

$$\hat{\mathbf{G}} = \vec{\nabla}\vec{B} = \partial_k B_i, \tag{1}$$

where B_i is the component of the magnetic field ($i = 1, 2, 3$). Because curl and divergence are both zero outside of source regions, according to Maxwell's equations, there will only be five independent elements, and the IMGT can then be written as a symmetric matrix

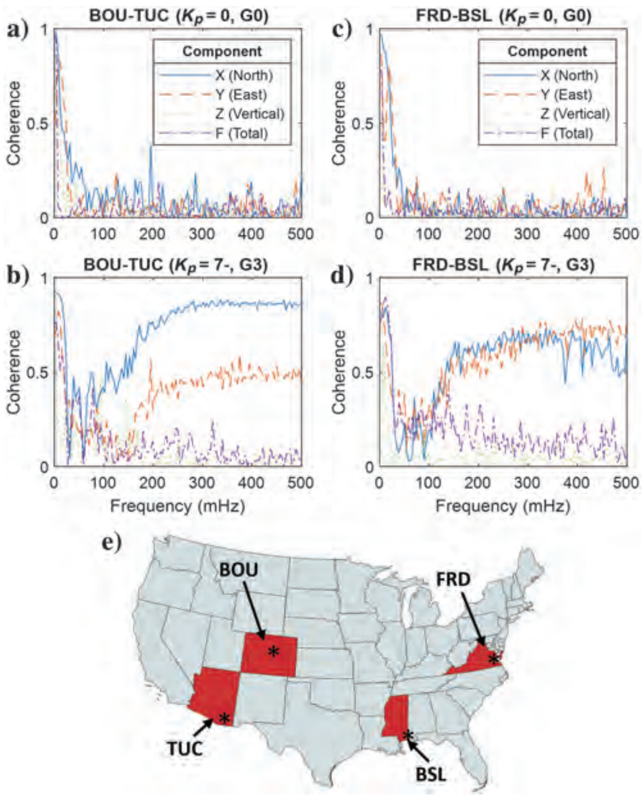

Figure 3. Coherence between magnetic reference stations during (a and c) geomagnetically quiet conditions, K_p index 0, and (b and d) a G3 geomagnetic storm, K_p index 7, at locations across the United States: (a) Boulder, CO, (b) Tucson, AZ, (c) Fredericksburg, VZ, and (d) NASA Stennis Space Center, MS. In quiet conditions, coherence is high at low frequencies for all components and falls off rapidly at frequencies >50 mHz. During geomagnetic storms, vertical and total field coherence falls off such as in quiet conditions but north and east components show enhanced coherence at higher frequencies.

$$\hat{\mathbf{G}} = \begin{pmatrix} B_{x,x} & B_{x,y} & B_{x,z} \\ B_{x,y} & B_{y,y} & B_{y,z} \\ B_{x,z} & B_{y,z} & -B_{x,x} - B_{y,y} \end{pmatrix} = \hat{\mathbf{G}}^T. \tag{2}$$

The double-subscript notation here refers to the partial derivative of the magnetic field component with respect to the direction (i.e., $B_{x,y} = (\partial B_x / \partial y)$).

Although magnetic gradiometry reduces distant noise sources and removes the need for secondary base stations to correct survey data, pointing error sensitivity remains. This motivated the introduction of the MGT invariants that are insensitive to rotation (Wiegert and Oeschger, 2005; Jin et al., 2020; Wang et al., 2023). Most applications of magnetic gradiometry assume the idealized IMGT, which will be, by definition, symmetric and traceless (Blakely, 1995). Actual magnetic gradiometer systems rely on finite-difference approximations of the IMGT, and, as a result, there will be differences between the idealized infinitesimal and the physical finite-differences MGT (FDMGT) (Xu et al., 2021). In practice, gradients are approximated by the separation-normalized difference between two or more magnetometers. Using the expressions of Xu et al. (2021) for a regular tetrahedron configuration (shown in Figure 4a), the FDMGT, $\mathbf{G}$, will then be of the form

$$\mathbf{G} = \frac{1}{d\sqrt{6}} \begin{pmatrix} \sqrt{2}(2B_{1x} - B_{2x} - B_{3x}) & \sqrt{2}(2B_{1y} - B_{2y} - B_{3y}) & \sqrt{2}(2B_{1z} - B_{2z} - B_{3z}) \\ \sqrt{2}(B_{1x} + B_{2x} - 2B_{3x}) & \sqrt{2}(B_{1y} + B_{2y} - 2B_{3y}) & \sqrt{2}(B_{1z} + B_{2z} - 2B_{3z}) \\ 3B_{4x} - B_{1x} - B_{2x} - B_{3x} & 3B_{4y} - B_{1y} - B_{2y} - B_{3y} & 3B_{4z} - B_{1z} - B_{2z} - B_{3z} \end{pmatrix}. \tag{3}$$

Here, we adopt the Xu et al. (2021) notation convention, where B_{1-4} are the four individual sensors in the tetrahedral configuration, and d is the separation distance between magnetometers.

ASYMMETRY OF THE FINITE-DIFFERENCE MGT

In contrast with the IMGT, the FDMGT may be neither traceless nor symmetric. Appendix A illustrates how asymmetry arises from the use of finite differences for a vertically separated gradiometer to first and second order in the dimensionless ratio ϵ of magnetometer separation distance d to source distance r (i.e., $\epsilon = d/r$) and how these errors relate to the distance from the dipole source. When the separation distance between magnetometers of the gradiometer is small compared with the distance from the magnetic source being characterized, which is the case in most applications of magnetic gradiometry, $\epsilon \ll 1$, and we need only account for first-order terms in ϵ. However, when characterizing nearby small anomalies, $\epsilon \approx 1$ and the higher-order terms cannot be ignored. This produces differences between the two equations, manifesting as an FDMGT asymmetry. Including higher-order terms enables a better approximation of the FDMGT, and higher-order derivatives contain information about local curvature. The greater the magnitude of the higher-order terms, the greater the curvatures, which results in a larger antisymmetric term. As a result, the relative size of the antisymmetric matrix term in equation 4 quantifies the local curvature of $\vec{B}$. In other words, the differences between the FDMGT and

IMGT capture information about magnetic field lines bending as they approach their dipolar source and can provide useful information about measured anomalies.

As shown previously, the differences between the IMGT $\hat{\mathbf{G}}$ and FDMGT $\mathbf{G}$ will appear as deviations from the expected symmetry of the IMGT. To highlight these deviations, it is useful to represent FDMGT as a sum of its symmetric part $\mathbf{G}_{\mathrm{S}}$ and its antisymmetric part $\mathbf{G}_{\mathrm{A}}$:

$$\mathbf{G} = \mathbf{G}_{\mathrm{S}} + \mathbf{G}_{\mathrm{A}} = \frac{\mathbf{G} + \mathbf{G}^T}{2} + \frac{\mathbf{G} - \mathbf{G}^T}{2}. \tag{4}$$

Functionally, the antisymmetric part represents errors arising from the magnetic gradiometer's physical size and geometry. It should be noted that, while $\mathbf{G}_{\mathrm{S}}$ will approach $\hat{\mathbf{G}}$, small differences can still be expected due to the finite-difference approximation.

The Frobenius norm provides a useful way of comparing matrices by measuring the average magnitude along mutually orthogonal directions in space. It is analogous to an L2 or Euclidian norm but for a matrix with a rank greater than one (Golub and Loan, 2013). The Frobenius norm of the symmetric part of the FDMGT, $\|\mathbf{G}_{\mathrm{S}}\|_F$, and the antisymmetric part $\|\mathbf{G}_{\mathrm{A}}\|_F$ can be expressed as (Golub and Loan, 2013)

$$\|\mathbf{G}_{\mathbf{A,S}}\|_F = \sqrt{\sum_{i=1}^{3}\sum_{j=1}^{3} |g_{A,S}, ij|^2}, \tag{5}$$

where $g_{S,ij}$ and $g_{A,ij}$ are the elements of $\mathbf{G}_{\mathbf{S}}$ and $\mathbf{G}_{\mathbf{A}}$, respectively.

We use the Frobenius norm of the symmetric and antisymmetric components of FDMGT to quantify how the gradiometer's finiteness (d) affects deviations from the symmetry of IMGT. Because the magnetometer separation distance equals the side length for a gradiometer with regular tetrahedron geometry, side length and d are used interchangeably in this paper, and it should be noted that this value is often called a baseline in the literature (e.g., Xu et al., 2021). In Figure 5, we plot $\|\mathbf{G}_{\mathbf{S}}\|_F$ and $\|\mathbf{G}_{\mathbf{A}}\|_F$ (left panel) and the ratio $\|\mathbf{G}_{\mathbf{A}}\|_F/\|\mathbf{G}_{\mathbf{S}}\|_F$ with increasing lateral distance (in the x-direction) from the source for three side lengths ($d = 0.25$ m, $d = 0.5$ m, and $d = 1$ m) (right panel). Both panels are calculated using a vertically oriented dipole from 1.5 m height. For small side lengths, the Frobenius norm is dominated by the symmetric part of the tensor. As the side length increases to larger values expected for physical gradiometer systems, the antisymmetric part grows and approaches the same amplitude as the symmetric part. The effective scale of the gradiometer may be described by the side length to distance-from-source ratio (see Appendix A). Because $\|\mathbf{G}_{\mathbf{A}}\|_F/\|\mathbf{G}_{\mathbf{S}}\|_F$ grows exponentially with the square of the length/distance ratio, this value may prove useful for determining the depth of a detected source. The $\|\mathbf{G}_{\mathbf{A}}\|_F/\|\mathbf{G}_{\mathbf{S}}\|_F$ ratio is small directly over the source but increases with increasing x-distance, producing two rings of high values encircling the source. We stress that the antisymmetric component of the finite-difference MGT we discuss in this paper results solely from the finite size of the gradiometer, compared with the scale of the magnetic anomalies analyzed. Noise and bias of individual magnetometers that comprise the gradiometer can also introduce an antisymmetric component; however, this is not the focus of our work. Note that while we have selected the Frobenius norm to demonstrate this deviation from symmetry, other invariants of the FDMGT will exhibit similar behavior.

In this study, we aim to compute or measure the MGT directly using four magnetometers — the minimum number needed to directly measure the gradients in all three directions. Although it is possible to reconstruct the full MGT using four magnetometers

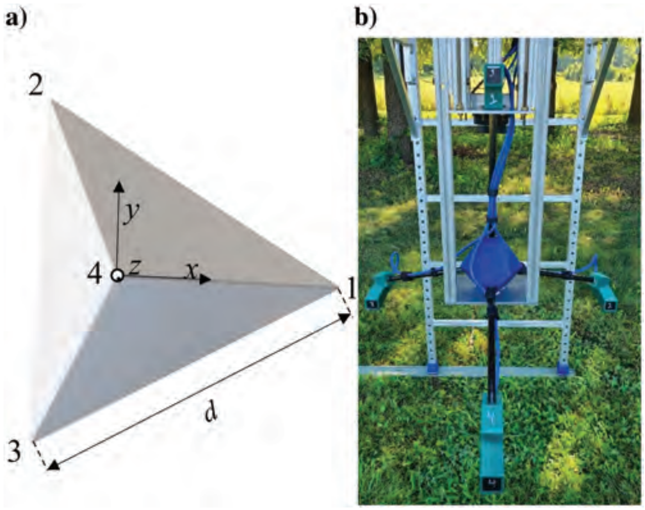

Figure 4. (a) Schematic of a regular tetrahedron-based triaxial magnetic gradiometer. Here, 1, 2, 3, and 4 are the positions of triaxial fluxgate magnetometers, each at the vertices of a regular tetrahedron. The side length (i.e., baseline or magnetometer separation distance) is d. Each magnetometer will have x-, y-, and z-components (B_{1x}, B_{1y}, B_{1z}, B_{2x}, etc.). (b) TetraMag magnetic gradiometer system. MEDA FVM400 triaxial fluxgate magnetometer sensor heads are in 3D-printed enclosures at the four vertices of a regular tetrahedron with $d = 0.5$ m side length.

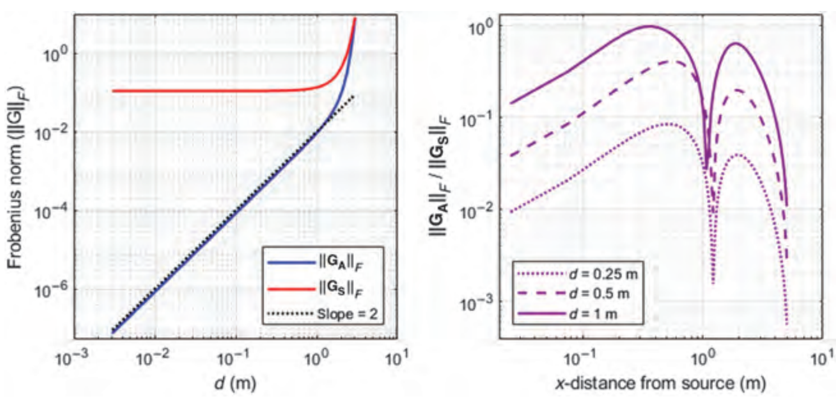

Figure 5. (a) Symmetric ($\|\mathbf{G}_{\mathbf{S}}\|_F$, red) and antisymmetric ($\|\mathbf{G}_{\mathbf{A}}\|_F$, blue) Frobenius norm components of FDMGT with increasing gradiometer side length d directly above the source and (b) the ratio $\|\mathbf{G}_{\mathbf{A}}\|_F/\|\mathbf{G}_{\mathbf{S}}\|_F$ with increasing x-distance from the source for three side lengths ($d = 0.25$ m, $d = 0.5$ m, and $d = 1$ m). Both panels are calculated for a vertically oriented dipole from 1.5 m height.

located on a horizontal plane (Xu et al., 2021), doing so requires leveraging the property that the magnetic field is divergence free. However, this assumption does not hold when finite differences are involved. Consequently, we limit our comparison to the regular tetrahedral geometry and the right-angle tetrahedron, as other geometries would require more than four magnetometers to capture all components of the MGT directly. Figure 6 shows the comparison between antisymmetric components of the FDMGT present in the regular and right-angle tetrahedron geometries, showing similar patterns of growth of the antisymmetric component with side length. It is worth noting that all geometries, including those not examined here, will produce an asymmetric component due to the finite nature of the measurements rather than the specific geometry of the array. Furthermore, the extent to which FDMGT measurements approximate ideal behavior (i.e., the amount by which they deviate from symmetry) will depend not only on the geometry of the gradiometer array but also its orientation with respect to the curvatures present in the magnetic field being interrogated.

INVARIANTS OF THE MGT

We seek to use matrix invariants to minimize the impact of rotational pointing errors for a finite triaxial gradiometer and explore which properties may be useful for small-size source detection and source parameter characterization. Invariants of interest for this study include previously described Frobenius norms, eigenvalues, determinants, and normalized source strengths (NSS) of the FDMGT.

By symmetric eigenvalue decomposition (spectral theorem), the FDMGT can be written in terms of its eigenvalues (Pedersen and Rasmussen, 1990)

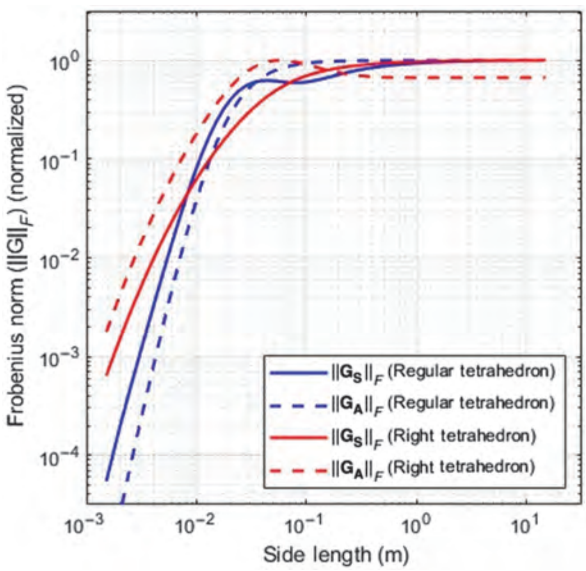

Figure 6. Normalized symmetric ($\|\mathbf{G_S}\|_F$, solid blue, solid red) and antisymmetric ($\|\mathbf{G_A}\|_F$, dashed blue, dashed red) Frobenius norm components of FDMGT for regular tetrahedron (blue) and right-angle tetrahedron (red) geometries with increasing gradiometer side length d directly above the source, calculated for a vertically oriented dipole from 1.5 m height.

$$\mathbf{G} = \mathbf{V}^T \begin{pmatrix} \lambda_1 & & \\ & \lambda_2 & \\ & & \lambda 3 \end{pmatrix} \mathbf{V}, \tag{6}$$

where matrix $\mathbf{V}$ contains mutually orthogonal eigenvectors $[\mathbf{v}1 \ \ \mathbf{v}2 \ \ \mathbf{v}3]$ and $\lambda 1, \lambda 2, \lambda 3$ are the corresponding eigenvalues $(\lambda 1 > \lambda 2 > \lambda 3)$.

If we interpret the MGT as defining a linear transformation, its determinant is the signed scaling factor for its volume and is invariant to rotation. However, this invariance is not guaranteed for the FDMGT because the accuracy of the finite-difference approximation can, in general, depend on the orientation of the physical gradiometer. To explore how the determinant will change with errors introduced by a regular tetrahedral magnetic gradiometer system, we need only consider the determinant of the symmetric part of the FDMGT, $|\mathbf{G_S}|$, which can be expressed as

$$|\mathbf{G_S}| = \lambda_1 \lambda_2 \lambda_3. \tag{7}$$

The determinant of the antisymmetric part $|\mathbf{G_A}|$ is zero by construction as antisymmetric matrices have a determinant of zero (Turnbull, 1928).

In addition to the traditional invariants described previously, we can combine eigenvalues in various ways. For this study, we focus on two eigenvalue combinations, λ_{C1} and λ_{C2}, which can be expressed as

$$\lambda_{C1} = \lambda_1^2 + \lambda_2^2 + \lambda_3^2, \tag{8}$$

$$\lambda_{C2} = \lambda_1^3 + \lambda_2^3 + \lambda_3^3. \tag{9}$$

Both λ_{C1} and λ_{C2} are rotationally invariant, as each term of the combinations is individually rotationally invariant. Here, λ_{C1} is sensitive to sums and λ_{C2} is sensitive to differences between λ_1 and λ_3, with approximately equal sensitivity to λ_2.

The NSS is another rotationally invariant quantity and can be expressed as a combination of eigenvalues λ_1, λ_2, and λ_3 (Clark, 2014):

$$\mathrm{NSS} = \sqrt{-\lambda_2^2 - \lambda_1 \lambda_3}. \tag{10}$$

The NSS peaks over compact 3D sources (Beiki et al., 2012; Clark, 2013, 2014), which is particularly interesting to this study for locating and characterizing small-size sources that produce small-amplitude signals, such as landmines and UXO.

It is also important to note that the FDMGT will still be subject to rotational variations of the physical gradiometer that may produce small changes in the expected invariant anomaly patterns.

DATA

Magnetic gradiometer system (TetraMag)

We have developed a magnetic gradiometer, called TetraMag, using four MEDA FVM400 triaxial fluxgate magnetometers whose data directly sample the full FDMGT. TetraMag is designed to detect small-size small-amplitude sources from very low altitudes (~2 m AGL) in the shallow critical zone. Vector magnetometers were chosen as the base sensors because gradient magnetometers constructed from scalar sensors suffer from limitations described in the scalar and vector magnetometry sections. In particular, by capturing gradients in multiple directions rather than only the gradient of the total field, vector gradiometers provide more comprehensive data that enables better source localization and improved anomaly interpretation, where total field gradiometers may potentially obscure anomalies from small-size small-amplitude sources. In addition, whereas both gradiometer types are sensitive to noise, the ability to analyze multiple components can sometimes help identify and mitigate noise sources more effectively for vector gradiometers versus total field gradiometers (von der Osten-Woldenburg, 2021). Their suboptimal performance is particularly significant when used at low altitudes, as the vertical gradient cannot be calculated reliably from total field gradiometers because the magnetic field is more complex at very low altitudes and noise levels are higher, particularly from anthropogenic sources (Gamey et al., 1997; Doll et al., 2000). Triaxial magnetic gradiometers, by comparison, can better discriminate between different sources of magnetic noise because they provide directional information. This makes it easier to filter out unwanted noise and focus on the relevant signals, improving the reliability of gradient measurements.

The four triaxial magnetometer sensor heads are in 3D-printed housings at the vertices of a regular tetrahedron, shown in Figure 4b. A regular tetrahedron was chosen based on the work of Xu et al. (2021), who showed that a regular tetrahedron configuration outperforms a right-angled tetrahedron for triaxial gradiometry purposes. When the distance between the source and observation point is more than 2.5 times the source object's diameter or length, the source's magnetic field may be treated as a dipole (Zhang et al., 2010; Xu et al., 2021). Our expected sources (landmines and UXO) have spatial scales on the order of 0.05–0.2 m, so we must measure them from at least 0.5 m height. To ensure that our ϵ is less than or equal to one, our magnetometer separation (baseline) must be a minimum of 0.5 m to accommodate very low-altitude measurements. Using this rationale, we selected the side length of $d = 0.5$ m for TetraMag.

Carbon fiber tubing connects each sensor head to a 3D-printed central hub. Aluminum supports help to control structural modes and allow TetraMag to be rigidly mounted to the survey platform of choice. Figure 4b shows TetraMag mounted on a rolling aluminum scaffold for test surveys.

Synthetic data

The forward model to generate synthetic data uses the physical geometry of TetraMag to calculate the expected vector components at each vertex location and then calculate the FDMGT **G** for a chosen sensor measuring height. The magnetic vector components for the dipole source were calculated using the methods presented by Smellie (1956) and modified by Oruç (2010). We assume magnetization is due to the earth's field only so that the components can be expressed as

$$B_x = 2p_0 \frac{r^2 l - 2r_x(r_x l + r_y m - z_0 n)}{r^4}, \tag{11}$$

$$B_y = 2p_0 \frac{r^2 m - 2r_y(r_x l + r_y m - z_0 n)}{r^4}, \tag{12}$$

$$B_z = -2p_0 \frac{r^2 n - 2z_0(r_x l + r_y m - z_0 n)}{r^4}, \tag{13}$$

where p_0 is the magnetic moment; z_0 is the depth below the plane of observation; l, m, and n are the direction cosines which depend on the magnetic inclination (I) and declination (D); and r is the distance between the dipole and measurement location, with r_x and r_y components in the x- and y-directions, respectively (Oruç, 2010).

At each measurement location, we use the centroid position of the tetrahedron to calculate the FDMGT **G** (equation 3). From the FDMGT, we calculate the values of each invariant of interest. Figure 7 shows a schematic visualization for a vertical source. Figure 7a shows the magnetic field lines of the source in a small survey area, with TetraMag to scale. Figure 7b shows the survey path in map view and centroid position where invariants are calculated. Figure 7c shows the visualization of a calculated example invariant at each pixel location. The pixels left in gridded format for demonstration purposes only.

Field data

Test data were collected using TetraMag mounted on an aluminum scaffold over a bar magnet (meant to approximate a metallic AP landmine) buried at 15 cm depth in a test sand bed and measured

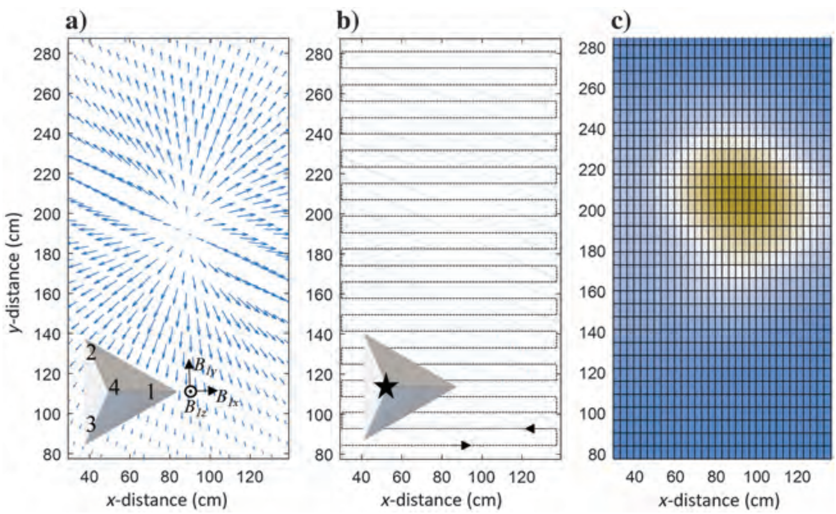

Figure 7. Conceptual survey geometry and FDMGT anomaly map. (a) Magnetic field lines for a vertical dipole in a small survey area, with TetraMag to scale (lower left). The terms B_{1x}, B_{1y}, and B_{1z} show example sampling directions for magnetometer 1. (b) Lawnmower-style survey patterns enable the calculation of **G** (equation 3), referenced to TetraMag's centroid (black star). (c) A conceptual visualization for an arbitrary **G** invariant, with the color of each pixel representing the value of the invariant at that location.

from 55 cm height. The test bed consists of a 300-gallon polyethylene containment tray filled with sand, located at the Paint Branch Turfgrass Research Facility in College Park, MD. The aluminum scaffold has magnetic resonance imaging (MRI)-safe wheels and an aluminum 8020 slider, allowing TetraMag to move in two directions, resulting in a lawnmower-style survey pattern shown in Figure 7b. Two 1D light detection and ranging units were used to keep track of the position of TetraMag during a survey and tied to individual magnetometer measurements via a shared clock on a Raspberry Pi 4 that simultaneously collected TetraMag and position data. The data were interpolated onto a spatial grid, with nodes at 1.25 mm spacing in x- and y-directions. We follow the data processing steps outlined in Merayo et al. (2000), enabling us to correct for sensor biases, normalize the axes using three scale factors, and account for three nonorthogonality angles, thereby establishing an intrinsic orthogonal system within the sensor. The components of the FDMGT were then calculated at each pixel point using the methods described for a regular tetrahedral gradiometer, as presented in Xu et al. (2021).

RESULTS

In this section, we present synthetic data for a vertically oriented dipole and a synthetic TetraMag to better demonstrate the expected difference between the calculated IMGT and FDMGT. We then investigate field data collected from our survey area, first comparing the average magnetic field (B_x, B_y, B_z) for its calculated and observed FDMGT and then examining their invariants.

We can visualize the synthetic data the same way we showed in Figure 7 to explore how the IMGT and FDMGT will differ as we change the pitch angle of TetraMag. Figure 8, columns 1–3, shows how the patterns of λ_1, λ_2, and λ_3 vary for IMGT and FDMGT when TetraMag is oriented parallel to the ground (IMGT 0° pitch, FDMT 0° pitch) and when it is rotated 30° with respect to the x-axis (FDMGT 30° pitch), each measured from 0.5 m height to the closest sensor. The dipole source is indicated by a white asterisk and buried at 15 cm depth to the top of the source. As expected, the visualized patterns for IMGT do not change with pitch rotation because the measurements are close to infinitesimal (side length = 0.000001 m), so their plots are omitted. The source is characterized by a single, symmetric ellipsoidal anomaly, with one local maximum for λ_1 and λ_2 and one local minimum for λ_3. For the FDMGT case, the source is characterized by a single, asymmetric ellipsoidal anomaly with one local maximum for λ_1 and a slightly triangular anomaly with one local maximum for λ_2. The characterization pattern for λ_3 differs the most from IMGT, with the source location surrounded by three ellipsoidal anomalies with local minima and centered at a maximum point between the three; λ_1 is surrounded by three ellipsoidal positive anomalies that shift location slightly as TetraMag is pitched 30°. It should be noted that the sign of the eigenvalues is arbitrary but their magnitude differs significantly from those of the surrounding synthetic survey area.

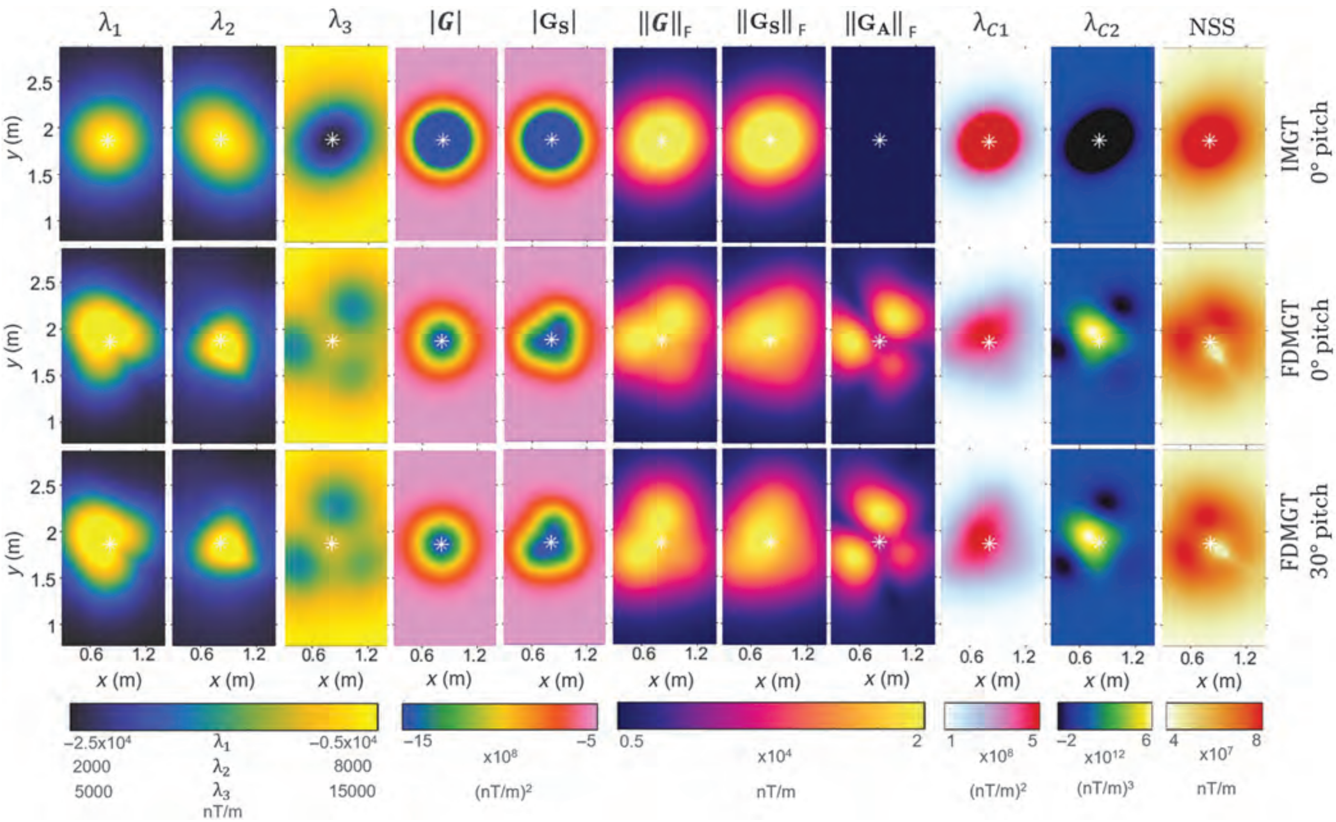

Figure 8. Maps of the eigenvalues (columns 1–3) and invariants (columns 4–11) calculated from synthetic data at two TetraMag orientations (pitch angles) for the IMGT and FDMGT. The white asterisk symbol indicates the source location for all plots. Eigenvalues λ_1, λ_2, and λ_3 are shown in columns 1–3. Determinant variations $|\mathbf{G}|$ and $|\mathbf{G_S}|$ are shown in columns 4 and 5. Frobenius norm variations $\|\mathbf{G_f}\|_F$, $\|\mathbf{G_S}\|_F$, and $\|\mathbf{G_A}\|_F$ are shown in columns 6–8. Variations of eigenvalue combinations 1 (λ_{C1}) and 2 (λ_{C2}) and NSS are shown in columns 9–11.

Figure 8, columns 4–5, shows how determinant values for the IMGT and FDMGT and their symmetric parts vary for the same TetraMag pitch angle. The $|\mathbf{G}|$ anomaly for the source is characterized by a single central circular low. For the $|\mathbf{G}|$ FDMGT case, the anomaly is characterized by a single circular low, whereas the $|\mathbf{G_S}|$ part reveals a more lobed low anomaly. The orientation of the triangular anomalous low pattern changes with changing TetraMag pitch angle.

In addition to asymmetry arising from the finite-difference approximation, any tilt will produce a distortion that results from having one of the sensors closer to the source than the others. The triangular distortion comes primarily from the geometry of the gradiometer. As TetraMag approaches a source, the sensors closest to the source will measure a higher amplitude signal, which manifests in the finite differences and, therefore, all derived quantities of the FDMGT.

Figure 8, columns 6–8, shows how Frobenius norm values for the IMGT and FDMGT, and the latter's symmetric and antisymmetric parts, vary for the same TetraMag pitch angle. The source is characterized by a circular anomalous high lobe for the IMGT, and a three-lobed anomaly high anomaly that blurs together in a triangular pattern for FDMGT. However, the pattern and amount of visual diffusivity depend on TetraMag pitch rotation for FDMGT. Here, $\|\mathbf{G_S}\|_F$ is also characterized by a three-lobed anomaly high anomaly that blurs together in a triangular pattern for FDMGT, plus an additional central high that is obscured by the white asterisk indicating the source position. The $\|\mathbf{G_A}\|_F$ values for FDMGT arise from the 0.5 m TetraMag side length and reveal three approximately circular anomalous highs, whose locations appear to match vertex locations of the triangular anomalous high seen in $\|G_S\|_F$, with a central low obscured by the source position asterisk.

Figure 8, columns 9–11, shows how λ_{C1}, λ_{C2}, and NSS values vary for IMGT and FDMT for the same TetraMag pitch angle. The source is characterized by a circular high anomaly for IMGT λ_{C1} and NSS, and by a circular low anomaly for λ_{C2}. The FDMGT source anomaly patterns differ from the IMGT case, where FDMGT λ_{C1} contains a semitriangular high anomaly whose northwestern edge (for 0° pitch) and western edge (for 30° pitch) has higher amplitude than the rest of the triangular anomaly. FDMGT λ_{C2} is characterized by a circular high anomaly surrounded by three circular low anomalies in a triangular configuration that shift in location with changing pitch angle. The FDMGT NSS pattern contains a trough-like low anomaly near the center of a higher amplitude ring, with one side of the ring containing higher amplitudes than the other side, depending on the pitch angle.

To compare the expected magnetic field of the dipole source to the observed, we calculated a separate synthetic data set using the setup parameters of our field area. Figure 9 shows the calculated (synthetic) and measured (field) values of the three components of the magnetic field B_x, B_y, and B_z. These synthetic data are distinct from those used for Figure 8, as these incorporate the magnetic moment and orientation of the testing bar magnet, magnetic inclination, and declination of the survey location, whiereas the synthetic data for Figure 8 are for a purely vertical source. It should be noted that the magnetization vector we used for the bar magnet in synthetic data calculations is only approximate, as we could not measure this in the field. As a result, the precise characterization pattern for each invariant anomaly can be expected to differ rotationally about the known source location. With this in mind, field and synthetic data patterns are considered a good fit if the general anomaly shape matches, and the amplitude and approximate position are consistent with expectations for the known source location. The fiberglass scaffold rolling tracks used for the field survey were not level due to local topography, which resulted in a nearly 30° tilt of TetraMag with respect to the y-axis (roll), which we accounted for in synthetic data calculations. Streak-like spurious features in the field data may be caused by inconsistent survey spacing, which maps into spatial features during interpolation (varying between 5 and 11 cm in the y-direction). From separate ground-based data, we observe that 1° differences in roll or pitch of TetraMag going in one direction versus the other in a lawnmower survey pattern can produce similar striping, so variations in orientation on this order from transect to transect may contribute to those seen in Figure 8. In addition, magnetic noise from nearby ferromagnetic clutter was observed in all three components, most significantly in B_y, and has been piecewise removed. Ghosting from this piecewise removal can be seen near $x = 50$ cm in the B_y plot.

Figure 10 shows eigenvalues λ_1, λ_2, and λ_3 (columns 1–3) for field and synthetic data. Synthetic λ_1 is characterized by two circular high anomalies, with the source location at the outer edge of the higher amplitude anomaly. Field λ_1 is characterized by a similar pattern as the synthetic data when we allow for rotation due to

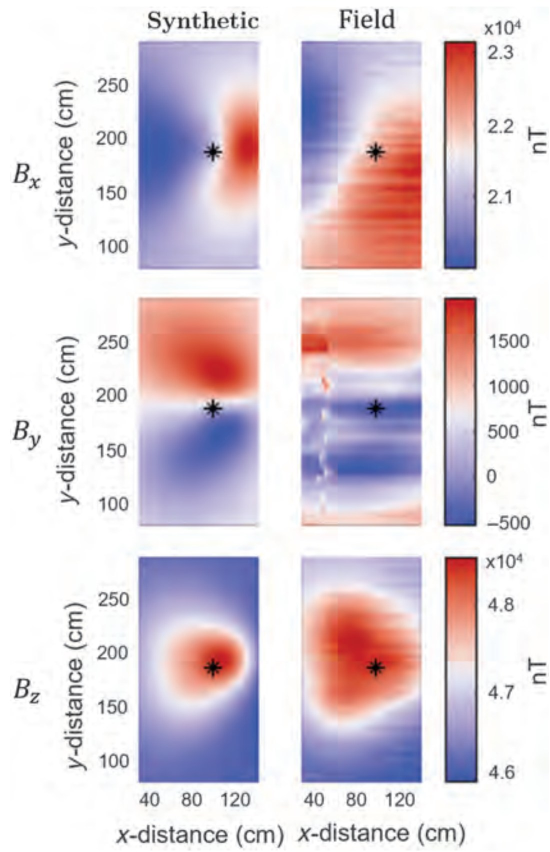

Figure 9. Average B_x, B_y, and B_z values for synthetic data and corresponding field data measured by TetraMag at 55 cm height, with 30° roll angle. The dipole source is indicated by a black asterisk and buried 15 cm in a test sand bed in College Park, MD. Synthetic data match the field magnetic inclination and declination values. Noise from magnetic clutter on the test scaffold has been piecewise removed from all components but is most apparent in B_y values, ghosting from which can be seen in the plot.

the approximated magnetization vector. However, there appears to be an additional anomalous low area in the field area that is not visible in the synthetic data, which may be a real signal from ferrous clutter unknown to us in the field. Here, λ_2 data are characterized by an ellipsoidal high anomaly in which the source is located and an ellipsoidal anomalous low anomaly next to the high anomaly. This pattern is consistent for field and synthetic data, though the field anomalies are more diffuse than the synthetic. The source is at the center of a single circular low anomaly for field and synthetic data. However, the radius of the circular low anomaly is larger in the field data than in the synthetic.

Figure 10 shows the determinant of the FDMGT ($|\mathbf{G}|$) (columns 4–5) and its symmetric part ($|\mathbf{G_S}|$). The source is characterized by a single circular low anomaly approximately centered at the source location in the synthetic data. The field data show some agreement with the synthetic data, as the source is centered in a circular low anomaly. Still, an additional ellipsoidal high anomaly is visible near the low anomaly, which may indicate the presence of ferrous clutter in the field area unaccounted for in synthetic data.

Figure 10 shows the Frobenius norm of the FDMGT $\|\mathbf{G}\|_F$ (columns 6–8), as well as its symmetric ($\|\mathbf{G_S}\|_F$) and antisymmetric ($\|\mathbf{G_A}\|_F$) parts. The expected patterns from the synthetic data approximately match the field data, especially for $\|\mathbf{G}\|_F$ and $\|\mathbf{G_S}\|_F$. The source is localized in the center of the anomalous positive lobe for $\|\mathbf{G}\|_F$ and $\|\mathbf{G_S}\|_F$, with finer resolution seen in $\|\mathbf{G_S}\|_F$ for synthetic and field data, though the lobe appears more elongated in the field data which is revealed to be a secondary positive lobe upon inspection in $\|\mathbf{G_S}\|_F$. The source is localized at the edge of a positive anomaly lobe in $\|\mathbf{G_A}\|_F$ for synthetic and field data, though two additional positive anomaly lobes are seen in the field data that are not present in the synthetic data, indicating less of a good fit which may indicate the presence of an additional source.

Figure 10 shows eigenvalue combinations λ_{C1}, λ_{C2}, and NSS (columns 9–11) for field and synthetic data. The source is localized in the center of a positive anomaly lobe for λ_{C1} and a negative anomaly lobe for λ_{C2} in synthetic and field data, though λ_{C1} is more elongated than the expected circular lobe in synthetic data. The positive anomaly lobe seen to the northwest of the negative lobe in λ_{C2} is present in synthetic and field data. There is a slight horizontal offset between the positive anomaly lobe in the synthetic data and field data, and an additional positive lobe is seen in the field data that is unseen in the synthetic data.

DISCUSSION

The impact of finiteness on FGMGT invariants

The finiteness of TetraMag introduces an antisymmetric component to the FDMGT. As discussed in the magnetic gradiometry section, $\|\mathbf{G_A}\|_F$ calculated above the center of a dipole grows with increasing side length and decreasing distance from a small compact magnetic source. Its ratio to $\|\mathbf{G_S}\|_F$ grows with the square of the side length, as shown in Figure 5. The side length of TetraMag also plays a significant role in the signal and expected invariant patterns derived from the FDMGT, which can be seen from the synthetic data. The FDMGT deviates from the IMGT, and the deviations are due to the finite approximation of gradients, which are captured in the antisymmetric portion of the FDMGT. These deviations are also seen in the field data, where TetraMag has a side length of 0.5 m.

However, the relative magnitude of the antisymmetric component of the FDGMT exhibits more complicated dependence on off-axis locations, reflecting the magnetization of the source. In Figure 11, we display $\|\mathbf{G_A}\|_F/\|\mathbf{G_S}\|_F$ at two flying heights,

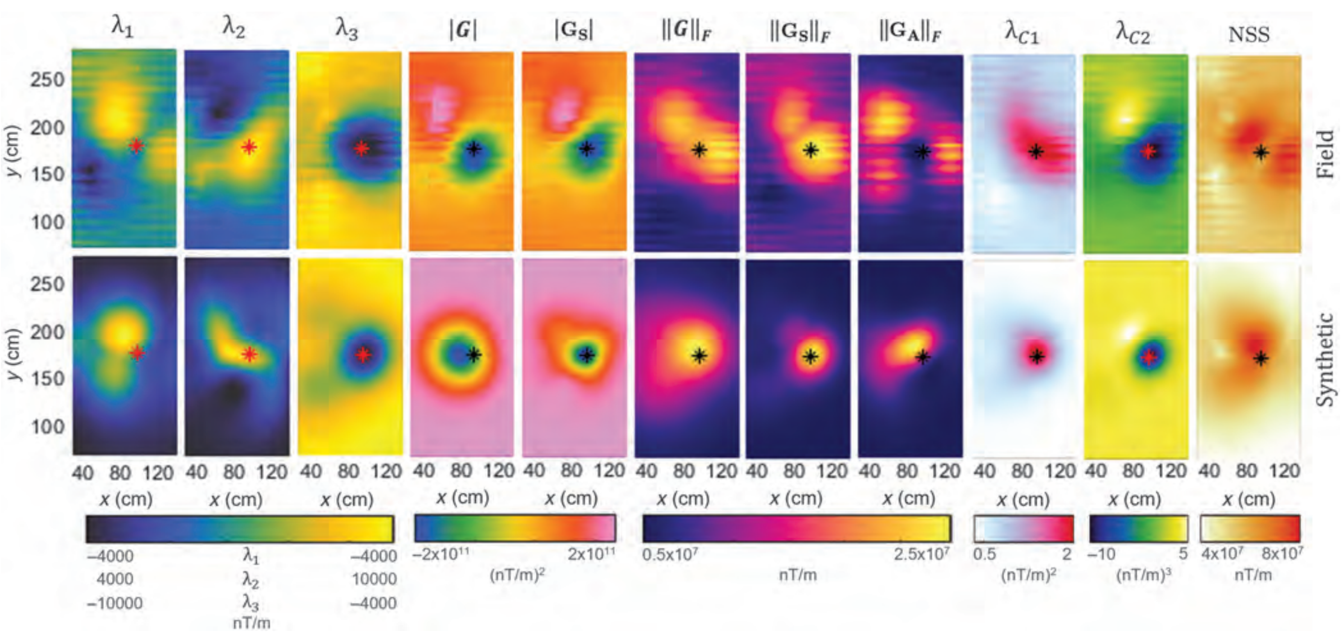

Figure 10. Maps of eigenvalues (columns 1–3) and invariants (columns 4–11) for field FDMGT data (top row) collected by TetraMag and synthetic FDMGT data (bottom row) calculated using TetraMag's geometry, tilt (30° roll angle), local magnetic conditions, and approximated source magnetization vector. Eigenvalues λ_1, λ_2, and λ_3 are shown in columns 1–3. Determinant variations $|\mathbf{G}|$ and $|\mathbf{G_S}|$ are shown in columns 4 and 5. Frobenius norm variations $\|\mathbf{G}\|_F$, $\|\mathbf{G_S}\|_F$, and $\|\mathbf{G_A}\|_F$ are shown in columns 6–8. Eigenvalue combinations 1 (λ_{C1}) and 2 (λ_{C2}) and NSS variations are shown in columns 9–11.

0.5 m (top row), corresponding to a ground-based survey, and 1.5 m (bottom row), corresponding to a low-altitude drone-based survey; side length is set equal to 0.5 m for both flying heights. Because orientation of the source magnetic dipole will affect the spatial variations of the magnetic field and therefore of the FDMGT itself. Figure 11 shows how the relative magnitude of the antisymmetric component of the FDGMT changes laterally for a dipping (left), horizontal (center), and vertical (right) source dipole orientation. When the magnetization is oriented vertically, the resulting pattern of $\|\mathbf{G_A}\|_F/\|\mathbf{G_S}\|_F$ has a small radius ring of high-amplitude values encircling the source location. The radius of this ring remains unchanged with changing flying height, suggesting it may be leveraged to precisely identify source locations. Unsurprisingly, the azimuthal symmetry of $\|\mathbf{G_A}\|_F/\|\mathbf{G_S}\|_F$ variations seen for the vertical magnetic dipole source does not persist for horizontally oriented or dipping magnetization vectors, for which $\|\mathbf{G_A}\|_F/\|\mathbf{G_S}\|_F$ variations exhibit more complicated lobate patterns. Although the largest antisymmetric components are still seen near the source, the high-amplitude ring seen for the vertical dipole becomes distorted and discontinuous, offering a simple way for vertical dipole signatures to be distinguished from dipping or horizontal ones.

Although the synthetic IMGT data presented here are rotationally invariant, consistent with the literature (Pedersen and Rasmussen, 1990; Schmidt and Clark, 2006; Oruç, 2010; Beiki et al., 2012), the FDMGT is still subject to rotational variations of the physical gradiometer, which produce small changes in the relative distances between the magnetometer positions and the magnetic sources in the subsurface, and therefore, introduce lateral variations in the expected pixel-to-pixel invariant pattern. The invariant pattern differences when TetraMag is rotated are most apparent in λ_1, λ_3, $|\mathbf{G_S}|$, $\|\mathbf{G}\|_F$, $\|\mathbf{G_S}\|_F$, $\|\mathbf{G_A}\|_F$, and λ_{C2}.

For $|\mathbf{G_S}|$ and $\|\mathbf{G_S}\|_F$, rotation of TetraMag results in a rotation of the vertices of the triangular anomaly pattern but the source location remains at the center of the negative anomaly for $|\mathbf{G_S}|$ and positive anomaly for $\|\mathbf{G_S}\|_F$. Similarly, the source remains located at the center of a positive anomaly lobe for λ_{C2} but there is an apparent shift in the surrounding positive anomaly lobe locations. The source location can still be identified in each of these cases, even with changes in surrounding lobe patterns. Note that this is for a simple dipole source, and more complex sources may exhibit more complex patterns. This has implications for flying height choice, ensuring the source may be treated as a simple dipole.

Pitch rotation of TetraMag results produce slight rotations in the location of anomaly lobes for λ_1, λ_2, λ_3, $|\mathbf{G_S}|$, $\|\mathbf{G}\|_F$, $\|\mathbf{G_S}\|_F$, $\|\mathbf{G_A}\|_F$, λ_{C1}, λ_{C2}, and NSS, for the FDMGT case. Because rotations of these patterns can also arise from differences in the source magnetization vector, it is important to include the yaw, pitch, and roll information of a magnetic gradiometer when performing inversions or computing synthetic data.

Invariants whose patterns are left largely unchanged when TetraMag is rotated include λ_{C1}, λ_2, and NSS, emphasizing that not all MGT invariants are equally invariant to rotation. Separating the full FDMGT into its symmetric and antisymmetric parts, however, overcomes some of the errors introduced by having a physical

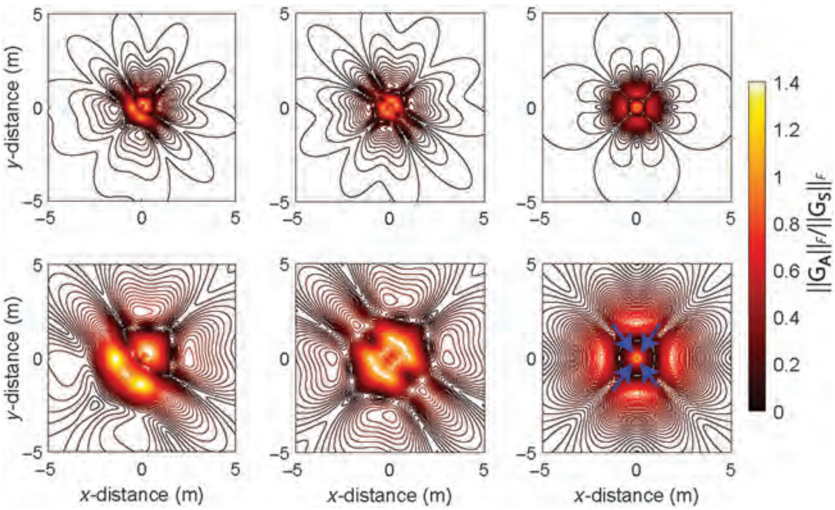

Figure 11. Ratio of $\|\mathbf{G_A}\|_F/\|\mathbf{G_S}\|_F$ at two flying heights, 0.5 m (top row), corresponding to a ground-based survey, and 1.5 m (bottom row), corresponding to a low-altitude drone-based survey. The side length is 0.5 m for both flying heights. The source is a magnetic dipole that is dipping (left), horizontal (center), or vertical (right). Although a vertical magnetization produces the most symmetric $\|\mathbf{G_A}\|_F/\|\mathbf{G_S}\|_F$ pattern around the source location, dipping orientations produce more complicated lobate patterns but still peak above the source.

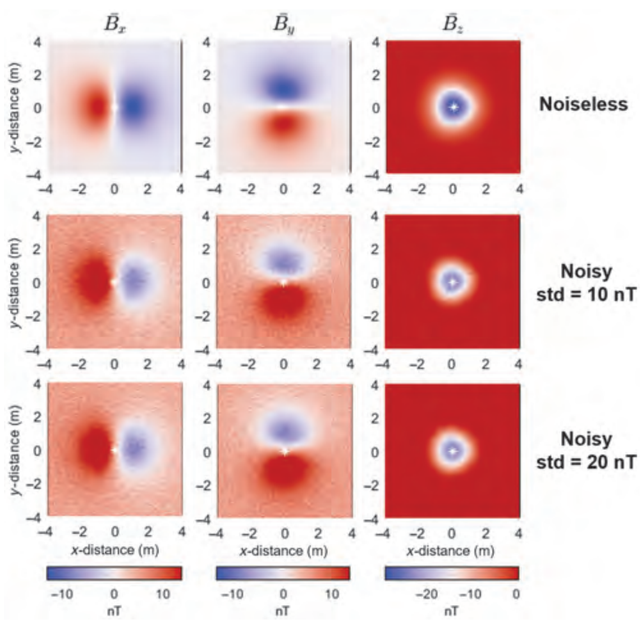

Figure 12. Average B_x, B_y, and B_z anomalies for a small (20 nT producing) vertically oriented source buried 0.1 m, from 1.5 m flying height, under different noise conditions. Here, average refers to the mean value for each component as seen by the gradiometer array (e.g., $B_x = (B_{1x} + B_{2x} + B_{3x} + B_{4x})/4$). The top row shows the noiseless case. The middle row shows when each magnetometer has random noise at the 10 nT std level. The bottom row shows when each magnetometer has random noise at the 20 nT level. The anomaly patterns remain resolvable for all three noise levels.

finite gradiometer and increases the localization resolution for the dipole source, especially for $|\mathbf{G}|$ and $\|\mathbf{G_S}\|_F$ and for the other invariants in this study as well. Although each included FDMGT invariant characterizes the source by their respective anomaly patterns, some invariants may be more useful for determining additional source parameters. They will be explored in future studies.

Sensitivity to noise

Because invariants of the MGT involve nonlinear combinations of the vector magnetic data, one can expect that they should have very different sensitivity to noise on individual magnetometers. To explore the impact of instrument noise on FDMGT data fidelity, we made a TetraMag synthetic data set for a vertically oriented dipole source with a small-amplitude anomaly (approximately 20 nT) buried at 0.1 m depth, calculated at 1.5 m flying height. We introduce additive white noise to each component of each vector magnetometer under three conditions: 0 nT (noiseless), 10 nT standard deviation (std), and 20 nT std levels. Figure 12 shows the average B_x, B_y, and B_z values across the four TetraMag sensors for the noiseless case (top row), 10 nT std case (middle row), and 20 nT std case. The noiseless case's anomaly pattern is recovered for 10 and 20 nT noise levels. Figure 13 shows how FDMGT invariants are impacted for the same noise conditions. The top row shows each invariant for noiseless conditions, whereas the middle and bottom rows show the 10 and 20 nT noise levels, respectively. When the noise level is approximately half the source anomaly amplitude, the anomaly patterns seen in the noiseless case are recovered for all invariants. When the noise reaches the same amplitude as the source anomaly, however, many of the invariant maps no longer show recognizable patterns (e.g., $|\mathbf{G}|$, $|\mathbf{G_S}|$, and λ_{C2}). Nevertheless, errors close to where the signal is high remain low for the Frobenius norm ($\|\mathbf{G}\|_F$, $\|\mathbf{G_S}\|_F$, and $\|\mathbf{G_A}\|_F$) and the NSS invariants. This indicates that not all FDMGT invariants effectively resolve small-size small-amplitude anomalies under varying noise conditions because some invariants exhibit greater sensitivity to noise compared with others. However, analysis of the FDMGT itself still offers valuable insights even in suboptimal noise environments.

Field data complications

Field data collection — even under ostensibly controlled conditions — invariably presents challenges not encountered in synthetic modeling. For example, inconsistent survey y-direction spacing in the field (varying from 5–11 cm) is mapped into spurious streak-like features during the interpolation step of the FDMGT processing. This may have contributed to some of the errors between the expected synthetic invariant patterns and field data patterns. In addition, the fiberglass scaffold rolling tracks used for the field survey were not level due to local topography, which resulted in a nearly 30° tilt of TetraMag with respect to the y-axis. All syn-

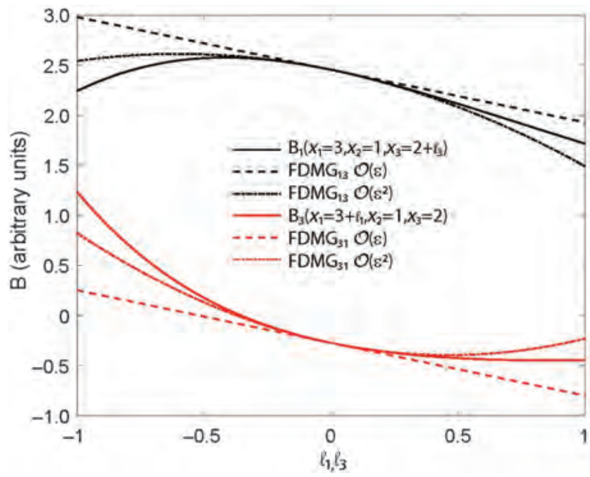

Figure 14. Magnetic field B versus separation distance d between magnetometers for the special case of a purely vertical magnetic moment. The $\hat{x}_3$ finite difference of the $\hat{x}_1$ component of the magnetic field ($\mathbf{G}_{13}$, solid black line) and the $\hat{x}_1$ finite difference of the $\hat{x}_3$-component of the magnetic field ($\mathbf{G}_{31}$, solid red line) are poorly approximated when only the first term in equations A-7 (black dashed) and A-13 (red dashed) is used. However, the inclusion of second-order terms in ϵ (dot-dashed lines) improves accuracy (see equations A-7 and A-13). Note that the dashed lines are parallel because of the symmetry of ∇B.

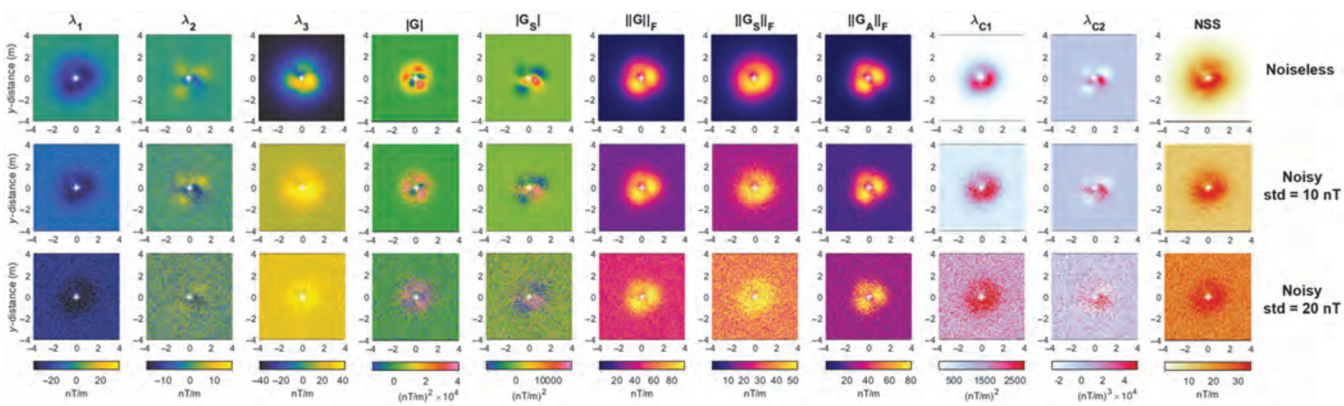

Figure 13. The FDMGT invariants for a small (20 nT producing) vertically oriented source buried 0.1 m, from 1.5 m flying height, under different noise conditions. The top row shows the noiseless case. The middle row shows when each magnetometer has random noise at the 10 nT std level. The bottom row shows when each magnetometer has random noise at the 20 nT level. Invariants include eigenvalues (λ_1, λ_2, λ_3), FDMGT determinant ($|\mathbf{G}|$), FDMGT symmetric determinant ($|\mathbf{G_S}|$), FDMGT Frobenius norm ($\|\mathbf{G}\|_F$), FDMGT symmetric Frobenius norm ($\|\mathbf{G_S}\|_F$), FDMGT antisymmetric Frobenius norm ($\|\mathbf{G_A}\|_F$), eigenvalue combinations 1 and 2 (λ_{C1}, λ_{C2}), and NSS.

thetic data have factored in this amount of tilt when calculating the FDMGT and its invariants.

CONCLUSION

This study explores how the finite size of magnetic gradiometers affects the symmetry and invariant properties of the FDMGT for magnetic anomalies produced by small buried objects. This contrasts with assumptions traditionally made based on the properties true for idealized IMGT, which should be symmetric and whose invariants should not be affected by rotations. Through synthetic tests and field data, we showed that these assumptions are invalid and FDMGT and IMGT should not be treated the same way. In addition, we showed that the effects of the finite size of a gradiometer can be assessed by decomposing the FDMGT into a symmetric and antisymmetric part.

The FDMGT properties analyzed in this study can enable rapid processing and interpretation of field data. Because most of the differences between IMGT and FDMGT are wrapped up in introducing an antisymmetric part to the MGT, using the symmetric part obviates the need for some of the more rigorous calibration efforts traditionally applied to magnetic survey data. This approach helps lay the foundation for UAV-based detection of small sources, and the relative stability of invariant patterns to rotations of TetraMag may enable the instrument to be rigidly mounted on the vehicle body. Because accurate gradiometer orientation information is crucial (see Figure 8), IMU data could, e.g., be used to correct for TetraMag tilt during inversion calculations. This effectively shifts the correction task to the data analysis side rather than the field operational side, where gimbals and other equipment would traditionally be used for the challenging task of always keeping the instrument level.

We showed that, theoretically, deviations from symmetry decrease with the square of the distance from the magnetic source (represented as a dipole) but can exhibit complicated spatial patterns depending on the orientation of the source's magnetization vector. Furthermore, we showed how the rotational dependence of invariants persists even when using the symmetric component of the FDMGT.

We explored the utility and benefit of leveraging the symmetric and antisymmetric parts of the FDMGT for locating and characterizing small-size small-amplitude anomaly sources in the shallow critical zone. In particular, the Frobenius norm ($\|G\|_F$), NSS, and eigenvalue combinations λ_{C1} and λ_{C2} enable high-resolution characterization of the anomaly patterns associated with small magnetic sources and may enable characterization of their source parameters, such as burial depth and magnetization orientation, which will be explored in follow-up studies. However, λ_{C1} and λ_{C2} were found to be more strongly affected by measurement noise compared with NSS and the Frobenius norm invariants. Building on theoretical frameworks from potential fields literature, we built and tested a regular tetrahedral triaxial magnetic gradiometer called TetraMag and demonstrated its ability to estimate the FDMGT, then compared each derived invariant's ability to localize the buried source with a complementary synthetic data set.

Future investigations will include multiple dipole-like sources, as well as ferromagnetic clutter, to ensure the robustness of the approach. Additional future work includes exploring the effect of single sources that deviate from dipoles for various source depths, sensor heights, and TetraMag yaw, pitch, and roll rotations. These data can build synthetic databases for machine learning (ML)-assisted inversion and source parameter estimation for small sources, such as landmines and UXO. Any ML synthetic training data should include rotations of the solid TetraMag structure to ensure all versions of the resulting invariant patterns are included as the network learns and updates. Characterizing real sources is also paramount for successful explosive remnants of war detection and/or identification tasks.

ACKNOWLEDGMENTS

We gratefully acknowledge the instrument design and fieldwork contributions of M. Taffel and A. Pick-Aluas, field assistance from staff at the Paint Branch Turfgrass Research Facility, D. Funk, 3D printing assistance and equipment manufacturing from UMD TerrapinWorks, and funding from NSF PFI-RP 2044611 and DoD NDSEG Fellowship.

DATA AND MATERIALS AVAILABILITY

Data associated with this research are available and can be obtained by contacting the corresponding author.

APPENDIX A

MAGNETIC FIELD FINITE DIFFERENCES

The magnetic field $\vec{B}$ at location $\vec{r}$ away from source regions can be written as the gradient of a scalar potential Φ:

$$\vec{B}(\vec{r}) = \vec{\nabla}\Phi(\vec{r}). \tag{A-1}$$

For a point dipole with magnetic moment $\vec{m}$, the magnetic field becomes (in SI units)

$$\vec{B} = \vec{\nabla}(\vec{m}\cdot\vec{\nabla}C_m r^{-1}), \tag{A-2}$$

where $C_m = \mu_0/4\pi$, μ_0 is the magnetic permeability of free space, and $r = |r| = \sqrt{\Sigma_k x_k^2}$. Remembering useful results that $\partial_i r = x_i/r$ and $\partial_i r^{-1} = -x_i r^{-3}$, and considering the special case of a purely vertical magnetic moment $\vec{m} = \sum_k m_0 \delta_{k3}\hat{e}_k$, the expression for the magnetic field simplifies to

$$\begin{aligned} \to B(\to r) &= -m_0 C_m \to \nabla(x_3 r^{-3}) \\ &= \frac{3m_0 C_m x_3}{r^5}\sum_i \left(x_i - \frac{r^2}{3x_i}\delta_{i3}\right)\hat{e}_i. \end{aligned} \tag{A-3}$$

The MGT $\vec{\nabla}\vec{B} = \partial_k B_i = \partial_k\partial_i\Phi$ is inherently symmetric because of the symmetry of second derivatives. However, when we measure the magnetic gradients, we actually measure the finite differences in the components of the magnetic field B_i across some physical separations $\vec{d}$. We can write this magnetic finite-differences matrix $\mathbf{G}$ as

$$G_{ij} = \frac{d}{|\rightarrow d|}\left[B_i\left(\sum_k x_k + d_j\delta_{kj}\hat{e}_k\right) - B_i\left(\sum_k x_k\hat{e}_k\right)\right]. \tag{A-4}$$

Let us consider taking the finite difference across a vertical separation, i.e., $\vec{d} = d_3\hat{e}_3$, of the $\hat{x}_1$-component of the magnetic field, and write the physical size of the magnetic gradiometer in terms of the vertical distance from the source, i.e., $d_3 = \epsilon x_3 = |d|$:

$$G_{13} = \frac{3m_0C_m}{\epsilon x_3}\left[\frac{1+\epsilon}{(\sum_k x_k^2(1+\epsilon\delta_{k3})^2)^{5/2}} - \frac{1}{(\Sigma_k x_k^2)^{5/2}}\right]x_3x_1. \tag{A-5}$$

When the scale of the magnetic gradiometer is small compared with the distance from the magnetic source being characterized, which is the case in most applications of magnetic gradiometry $\epsilon \ll 1$, we need only account for terms of the first order in ϵ. However, in our use case of characterizing magnetic anomalies that are small in amplitude and small in spatial extent, ϵ can approach unity, and we cannot neglect $\mathcal{O}(\epsilon^2)$ terms (see Figure 14). Therefore, we proceed by expanding the terms to second order in ϵ using the binomial approximation: $(1+\epsilon)^\alpha \approx 1 + \alpha\epsilon + (\alpha/2)(\alpha-1)\epsilon^2$. After some algebra, the first term in equation A-5 becomes

$$\frac{(1+\epsilon)}{r^5}[1+(2\epsilon+\epsilon^2)x_3^2/r^2]^{-5/2} \approx \frac{1}{r^5}\left[1+\left(1-5\frac{x_3^2}{r^2}\right)\epsilon - \frac{5}{2}\frac{x_3^2}{r^2}\left(3-7\frac{x_3^2}{r^2}\right)\epsilon^2 + \mathcal{O}(\epsilon^3)\right]. \tag{A-6}$$

The entire expression for the vertical finite difference of the $\hat{x}_1$-component of the magnetic field (equation A-5) then simplifies to

$$G_{13} = \frac{3m_0C_m}{r^5}\left[\left(1-5\frac{x_3^2}{r^2}\right) - \frac{5}{2}\frac{x_3^2}{r^2}\left(3-7\frac{x_3^2}{r^2}\right)\epsilon + \mathcal{O}(\epsilon^2)\right]x_1. \tag{A-7}$$

Now, we turn our attention to the finite difference in the $\hat{x}_i$-direction (i.e., $\vec{d} = d_i\hat{e}_i = \epsilon x_i\hat{e}_1$) of the vertical component of the magnetic field:

$$G_{3i} = \frac{3m_0C_m}{\epsilon x_i}\left[\frac{x_3 - \frac{1}{3x_3}\sum_k x_k^2(1+\epsilon\delta_{ki})^2}{(\sum_k x_k^2(1+\epsilon\delta_{ki})^2)^{5/2}} - \frac{x_3 - \frac{r^2}{3x_3}}{(\Sigma_k x_k^2)^{5/2}}\right]x_3. \tag{A-8}$$

Simplifying the summation terms using r,

$$\sum_k x_k^2(1+\epsilon\delta_{ki})^2 = r^2\left[1+(2\epsilon+\epsilon^2)\frac{x_i^2}{r^2}\right], \tag{A-9}$$

and using the binomial approximation to second order in ϵ,

$$\left(\sum_k x_k^2(1+\epsilon\delta_{ki})^2\right)^{-5/2} \approx r^{-5}\left[1-5\frac{x_i^2}{r^2}\epsilon - \frac{5x_i^2}{2r^2}\left(1-7\frac{x_i^2}{r^2}\right)\epsilon^2 + \mathcal{O}(\epsilon^3)\right], \tag{A-10}$$

we can approximate equation A-8 to read

$$G_{3i} \approx \frac{3m_0C_m}{\epsilon x_i r^5}\left[\left(x_3 - \frac{r^2}{3x_3} - (2\epsilon+\epsilon^2)\frac{x_i^2}{3x_3}\right) * \left[1-5\frac{x_i^2}{r^2}\epsilon - \frac{5x_i^2}{2r^2}\left(1-7\frac{x_i^2}{r^2}\right)\epsilon^2\right] - \left(x_3 - \frac{r^2}{3x_3}\right)\right]x_3. \tag{A-11}$$

After some algebra, the preceding expression simplifies further:

$$G_{3i} \approx \frac{3m_0C_m}{\epsilon x_i r^5}\left[\left(\frac{r^2}{3x_3} - x_3\right)\left[5\frac{x_i^2}{r^2}\epsilon + \frac{5x_i^2}{2r^2}\left(1-7\frac{x_i^2}{r^2}\right)\epsilon^2\right] - (2\epsilon+\epsilon^2)\frac{x_i^2}{3x_3}\left(1-5\frac{x_i^2}{r^2}\epsilon\right)\right]x_3. \tag{A-12}$$

Rearranging by order of ϵ, we arrive at

$$G_{3i} = \frac{3m_0C_m}{r^5}\left[\left(1-5\frac{x_3^2}{r^2}\right) + \left(\frac{1}{2} - \frac{15x_i^2}{6r^2} - \frac{5x_3^2}{2r^2} + \frac{35x_i^2x_3^2}{2r^4}\right)\epsilon + \mathcal{O}(\epsilon^2)\right]x_i. \tag{A-13}$$

Comparing equations A-7 and A-13, we can see that when $\epsilon \ll 1$, the two are equal, as we expected from the symmetry of second derivatives of the scalar potential. However, when characterizing nearby small-size anomalies, $\epsilon \approx 1$ and the higher order terms produce differences between the two equations. This manifests as an asymmetry in the finite-differences magnetic gradient matrix. The amplitude of the asymmetry is proportional to the amplitude of the higher-order spatial derivatives of $\vec{B}$. The ratio of the second- to first-order spatial derivatives of a vector field is related to the curvature of the field, with larger curvatures corresponding to stronger second-order spatial derivatives. When we express the FDMGT as a sum of symmetric and antisymmetric matrices, the relative size of the antisymmetric matrix quantifies the local curvature of $\vec{B}$. Because higher-order spatial derivatives — i.e., terms higher order in ϵ — fall off more quickly with distance r, the curvature of $\vec{B}$ and the size of the antisymmetric component of FDMGT can serve as a proxy for the gradiometer's proximity to a localized magnetic source.

REFERENCES

Accomando, F., A. Bonfante, M. Buonanno, J. Natale, S. Vitale, and G. Florio, 2023, The drone-borne magnetic survey as the optimal strategy for high-resolution investigations in presence of extremely rough terrains: The case study of the Taverna San Felice Quarry Dike: Journal of Applied Geophysics, **217**, 105186, doi: 10.1016/j.jappgeo.2023.105186.

Accomando, F., A. Vitale, A. Bonfante, M. Buonanno, and G. Florio, 2021, Performance of two different flight configurations for drone-borne magnetic data: Sensors, **21**, 5736, doi: 10.3390/s21175736.

Alqudsi, Y. S., A. S. Alsharafi, and A. Mohamed, 2021, A review of airborne landmine detection technologies: Unmanned aerial vehicle-based approach: International Congress of Advanced Technology and Engineering, 1–5.
Azry, H. A., H. A. Zubaidy, S. Webster, W. Witham, and D. Isles, 1993, Exploration for cyprus style copper deposits, Sultanate of Oman: A case history: Exploration Geophysics, **24**, 315–321, doi: 10.1071/EG993315.
Barnawi, A., N. Kumar, I. Budhiraja, K. Kumar, A. Almansour, and B. Alzahrani, 2022, Deep reinforcement learning based trajectory optimization for magnetometer-mounted UAV to landmine detection: Computer Communications, **195**, 441–450, doi: 10.1016/j.comcom.2022.09.002.
Barrère, C., J. Ebbing, and L. Gernigon, 2011, 3-D density and magnetic crustal characterization of the southwestern Barents Shelf: Implications for the offshore prolongation of the Norwegian Caledonides: Geophysical Journal International, **184**, 1147–1166, doi: 10.1111/j.1365-246X.2010.04888.x.
Baur, J., G. Steinberg, A. Nikulin, K. Chiu, and T. S. de Smet, 2020, Applying deep learning to automate UAV-based detection of scatterable landmines: Remote Sensing, **12**, 859–16, doi: 10.3390/rs12050859.
Beiki, M., D. A. Clark, J. R. Austin, and C. A. Foss, 2012, Estimating source location using normalized magnetic source strength calculated from magnetic gradient tensor data normalized source strength: Geophysics, **77**, no. 6, J23-J37, doi: 10.1190/geo2011-0437.1.
Billings, S. D., L. R. Pasion, and D. W. Oldenburg, 2002, Discrimination and identification of UXO by geophysical inversion. Phase II: Inversion of total-field magnetics: USACE Engineer Research and Development Center.
Birch, F. S., 1984, Bedrock depth estimates from ground magnetometer profiles: Groundwater, **22**, 427–432, doi: 10.1111/j.1745-6584.1984.tb01413.x.
Blakely, R., 1995, Potential theory in gravity and magnetic applications: Cambridge University Press.
Bott, M. H. P., and R. A. Smith, 1958, The estimation of the limiting depth of gravitating bodies: Geophysical Prospecting, **6**, 1–10, doi: 10.1111/j.1365-2478.1958.tb01639.x.
Clark, D. A., 2013, New methods for interpretation of magnetic vector and gradient tensor data II: Application to the Mount Leyshon anomaly, Queensland, Australia: Exploration Geophysics, **44**, 114–127, doi: 10.1071/EG12066.
Clark, D. A., 2014, Corrigendum to new methods for interpretation of magnetic vector and gradient tensor data I: Eigenvector analysis and the normalized source strength: Exploration Geophysics, **45**, 267–282, doi: 10.1071/EG12020_CO.
Cordell, L., and V. J. S. Grauch, 1985, Mapping basement magnetization zones from aeromagnetic data in the San Juan Basin, New Mexico: SEG.
Doll, W. E., J. E. Nyquist, L. P. Beard, and T. J. Gamey, 2000, Airborne geophysical surveying for hazardous waste site characterization on the Oak Ridge reservation, Tennessee: Geophysics, **65**, 1372–1387, doi: 10.1190/1.1444828.
Døssing, A., H. R. Jackson, J. Matzka, I. Einarsson, T. M. Rasmussen, A. V. Olesen, and J. M. Brozena, 2013, On the origin of the Amerasia Basin and the high arctic large igneous province-results of new aeromagnetic data: Earth and Planetary Science Letters, **363**, 219–230, doi: 10.1016/j.epsl.2012.12.013.
Florsch, N., C. Camerlynck, M. Kammenthaler, and F. Muhlach, 2018, Everyday applied geophysics 2: Electromagnetics and magnetics: ISTE Press Limited-Elsevier Incorporated.
Foss, C., 2020, Magnetic data enhancements and depth estimation, *in* H. K. Gupta, ed., Encyclopedia of solid earth geophysics: Springer, 1–14.
Gallardo, L. A., S. L. Fontes, M. A. Meju, M. P. Buonora, and P. P. D. Lugao, 2012, Robust geophysical integration through structure-coupled joint inversion and multispectral fusion of seismic reflection, magnetotelluric, magnetic, and gravity images: Example from Santos Basin, Offshore Brazil: Geophysics, **77**, no. 5, B237-B251, doi: 10.1190/geo2011-0394.1.
Gamey, T. J., J. S. Holladay, and R. Mahler, 1997, Airborne measured analytic signal for UXO detection: 10th EEGS Symposium on the Application of Geophysics to Engineering and Environmental Problems, cp-204.
Gavazzi, B., P. L. Maire, J. M. de Lépinay, P. Calou, and M. Munschy, 2019, Fluxgate three-component magnetometers for cost-effective ground, UAV and airborne magnetic surveys for industrial and academic geoscience applications and comparison with current industrial standards through case studies: Geomechanics for Energy and the Environment, **20**, 100117, doi: 10.1016/j.gete.2019.03.002.
Gavazzi, B., P. L. Maire, M. Munschy, and A. Dechamp, 2016, Fluxgate vector magnetometers: A multisensor device for ground, UAV, and airborne magnetic surveys: The Leading Edge, **35**, 795–797, doi: 10.1190/tle35090795.1.
Ghalenoei, E., J. Dettmer, M. Y. Ali, and J. W. Kim, 2021, Gravity and magnetic joint inversion for basement and salt structures with the reversible-jump algorithm: Geophysical Journal International, **227**, 746–758, doi: 10.1093/gji/ggab251.
Golub, G. H., and C. F. V. Loan, 2013, Matrix computations: JHU Press.
Gunn, P. J., and M. C. Dentith, 1997, Magnetic responses associated with mineral deposits: AGSO Journal of Australian Geology and Geophysics, **17**, 145–158.
Hamlyn, J., 2022, Magnetometry method: CRC Press.
Hinze, W. J., R. R. B. V. Frese, R. V. Frese, and A. H. Saad, 2013, Gravity and magnetic exploration: Principles, practices, and applications: Cambridge University Press.
Jin, H., J. Guo, H. Wang, Z. Zhuang, J. Qin, and T. Wang, 2020, Magnetic anomaly detection and localization using orthogonal basis of magnetic tensor contraction: IEEE Transactions on Geoscience and Remote Sensing, **58**, 5944–5954, doi: 10.1109/TGRS.2020.2973322.
Kappler, K. N., D. D. Schneider, L. S. MacLean, and T. E. Bleier, 2017, Identification and classification of transient pulses observed in magnetometer array data by time-domain principal component analysis filtering: Earthquake Science, **30**, 193–207, doi: 10.1007/s11589-017-0191-6.
Liu, H., H. Dong, J. Ge, and Z. Liu, 2022, An overview of sensing platform-technological aspects for vector magnetic measurement: A case study of the application in different scenarios: Measurement, **187**, 110352, doi: 10.1016/j.measurement.2021.110352.
Mandea, M., and A. Chambodut, 2020, Geomagnetic field processes and their implications for space weather: Surveys in Geophysics, **41**, 1611–1627, doi: 10.1007/s10712-020-09598-1.
Merayo, J. M., P. Brauer, F. Primdahl, J. R. Petersen, and O. V. Nielsen, 2000, Scalar calibration of vector magnetometers: Measurement Science and Technology, **11**, 120–132, doi: 10.1088/0957-0233/11/2/304.
Michelena, M. D., R. Kilian, M. Ángel Rivero, S. F. Romero, F. Ríos, J. L. Mesa, and A. Oyarzún, 2022, Magnetometric surveys for the non-invasive surface and subsurface interpretation of volcanic structures in planetary exploration, a case study of several volcanoes in the Iberian Peninsula: Remote Sensing, **14**, 2039, doi: 10.3390/rs14092039.
Mu, Y., X. Zhang, W. Xie, and Y. Zheng, 2020, Automatic detection of near-surface targets for unmanned aerial vehicle (UAV) magnetic survey: Remote Sensing, **12**, 452, doi: 10.3390/rs12030452.
Munschy, M., D. Boulanger, P. Ulrich, and M. Bouiflane, 2007, Magnetic mapping for the detection and characterization of UXO: Use of multi-sensor fluxgate 3-axis magnetometers and methods of interpretation: Journal of Applied Geophysics, **61**, 168–183, doi: 10.1016/j.jappgeo.2006.06.004.
Nikulin, A., T. deSmet, A. Puliaiev, V. Zhurakhov, S. Fasullo, G. Chen, I. Spiegel, and K. Cappuccio, 2020, Automated UAS aeromagnetic surveys to detect MBRL unexploded ordnance: The Journal of Conventional Weapons Destruction, **24**, 13.
Nogi, Y., J. A. Tarduno, and W. W. Sager, 1995, Inferences about the nature and origin of basalt sequences from the cretaceous mid-pacific mountains (sites 865 and 866), as deduced from downhole magnetometer logs: Proceedings of the Ocean Drilling Program, Scientific Results, 381–388.
Olsen, N., F. Primdahl, L. Tøffner-Clausen, T. Sabaka, P. Brauer, J. Merayo, J. Jørgensen, O. Nielsen, F. Primdahl, J. M. Léger, and T. Risbo, 2003, Calibration of the Ørsted vector magnetometer: Earth, Planets and Space, **55**, 11–18, doi: 10.1186/BF03352458.
Oruç, B., 2010, Location and depth estimation of point-dipole and line of dipoles using analytic signals of the magnetic gradient tensor and magnitude of vector components: Journal of Applied Geophysics, **70**, 27–37, doi: 10.1016/j.jappgeo.2009.10.002.
Pang, H., S. Luo, Q. Zhang, J. Li, D. Chen, M. Pan, and F. Luo, 2013, Calibration of a fluxgate magnetometer array and its application in magnetic object localization: Measurement Science and Technology, **24**, 075102, doi: 10.1088/0957-0233/24/7/075102.
Pasion, L. R., S. D. Billings, and D. W. Oldenburg, 2003, Joint and cooperative inversion of magnetic and time domain electromagnetic data for the characterization of UXO: 16th EEGS Symposium on the Application of Geophysics to Engineering and Environmental Problems, cp-190.
Pedersen, L. B., and T. M. Rasmussen, 1990, The gradient tensor of potential field anomalies: Some implications on data collection and data processing of maps: Geophysics, **55**, 1558–1566, doi: 10.1190/1.1442807.
Peters, L. J., 1949, The direct approach to magnetic interpretation and its practical application: Geophysics, **14**, 290–320, doi: 10.1190/1.1437537.
Pham, L., and A. Desimone, 2017, Vibration rectification in MEMS accelerometers: Analog Devices, Inc.
Pylvänäinen, T., 2008, Automatic and adaptive calibration of 3D field sensors: Applied Mathematical Modelling, **32**, 575–587, doi: 10.1016/j.apm.2007.02.004.
Reid, A. B., J. M. Allsop, H. Granser, A. J. Millett, and I. W. Somerton, 1990, Magnetic interpretation in three dimensions using Euler deconvolution: Geophysics, **55**, 80–91, doi: 10.1190/1.1442774.
Riddihough, R. P., 1971, Diurnal corrections to magnetic surveys — An assessment of errors: Geophysical Prospecting, **19**, 551–567, doi: 10.1111/j.1365-2478.1971.tb00900.x.
Santos, A. C., W. U. Mohriak, M. C. Geraldes, W. H. Santos, C. F. Ponte-Neto, and N. Stanton, 2019, Compiled potential field data and seismic surveys across the eastern Brazilian continental margin integrated with new magnetometric profiles and stratigraphic configuration for Trindade Island, South Atlantic, Brazil: International Geology Review, **61**, 1728–1744, doi: 10.1080/00206814.2018.1542634.
Schmidt, P., and D. Clark, 2000, Advantages of measuring the magnetic gradient tensor: Preview, **85**, 26–30.

Schmidt, P. W., and D. A. Clark, 2006, The magnetic gradient tensor: Its properties and uses in source characterization: The Leading Edge, **25**, 75–78, doi: 10.1190/1.2164759.

Shahsavani, H., 2019, Comparison of a low-cost magneto-inductive magnetometer with a proton magnetometer: A case study on the Galali iron ore deposit in Western Iran: Near Surface Geophysics, **17**, 69–84, doi: 10.1002/nsg.12026.

Smellie, D. W., 1956, Elementary approximations in aeromagnetic interpretation: Geophysics, **21**, 1021–1040, doi: 10.1190/1.1438294.

Smith, R. A., 1959, Some depth formulae for local magnetic and gravity anomalies: Geophysical Prospecting, **7**, 55–63, doi: 10.1111/j.1365-2478.1959.tb01453.x.

Thompson, D. T., 1982, EULDPH: A new technique for making computer-assisted depth estimates from magnetic data: Geophysics, **47**, 31–37, doi: 10.1190/1.1441278.

Turnbull, H. W., 1928, The theory of determinants, matrices, and invariants: Blackie and Son.

von der Osten-Woldenburg, H., 2021, Magnetic gradiometry, *in* H. K. Gupta, ed., Encyclopedia of solid earth geophysics: Springer, 1–6.

Wang, H., T. Meng, W. Luo, R. Yang, H. Liu, J. Ge, and H. Dong, 2023, Overhauser sensor array based 3-D magnetic gradiometer for the detection of shallow subsurface unexploded ordnance: IEEE Transactions on Instrumentation and Measurement, **72**, 1–11, doi: 10.1109/TIM.2023.3277942.

Wiegert, R., and J. Oeschger, 2005, Generalized magnetic gradient contraction based method for detection, localization and discrimination of underwater mines and unexploded ordnance: Proceedings of OCEANS 2005 MTS/IEEE, 1325–1332.

Xu, L., N. Zhang, L. Fang, H. Chen, P. Lin, and C. Lin, 2021, Simulation analysis of magnetic gradient full-tensor measurement system: Mathematical Problems in Engineering, **2021**, 6688364, doi: 10.1155/2021/6688364.

Yarger, H. L., R. R. Robertson, and R. L. Wentland, 1978, Diurnal drift removal from aeromagnetic data using least squares: Geophysics, **43**, 1148–1156, doi: 10.1190/1.1440884.

Yoo, L. S., J. H. Lee, S. H. Ko, S. K. Jung, S. H. Lee, and Y. K. Lee, 2020, A drone fitted with a magnetometer detects landmines: IEEE Geoscience and Remote Sensing Letters, **17**, 2035–2039, doi: 10.1109/LGRS.2019.2962062.

Yoo, L.-S., J.-H. Lee, Y.-K. Lee, S.-K. Jung, and Y. Choi, 2021, Application of a drone magnetometer system to military mine detection in the demilitarized zone: Sensors, **21**, 3175, doi: 10.3390/s21093175.

Zeyen, H., and J. Pous, 1993, 3-D joint inversion of magnetic and gravimetric data with a priori information: Geophysical Journal International, **112**, 244–256, doi: 10.1111/j.1365-246X.1993.tb01452.x.

Zhang, C., C. Xiao, J. Gao, and G. Zhou, 2010, Experimental study on the applicability of the magnetic dipole model of magnetic objects: Journal of Applied Basic and Engineering Science, **18**, 862–866.

Zuo, B., L. Wang, and W. Chen, 2017, Full tensor eigenvector analysis on air-borne magnetic gradiometer data for the detection of dipole-like magnetic sources: Sensors, **17**, 1976, doi: 10.3390/s17091976.

Biographies and photographs of the authors are not available.